Local Heat Transfer to an Evaporating Sessile Droplet in an Electric Field

M.J. Gibbons[1], C.M. Howe[1], P. Di Marco[2], A.J. Robinson[1]

[1] Trinity College Dublin, Dublin, Ireland
[2] DESTEC, University of Pisa, Pisa, Italy

E-mail: migibbon@tcd.ie

Abstract.

Local heat transfer of an evaporating sessile droplet under a static electric field is an underdeveloped topic. In this research an 80 µl water droplet is placed in the centre of a 25 µm thick stainless steel substrate. A static electric field is applied by an electrode positioned 10 mm above the substrate. A high speed thermal imaging camera is placed below the substrate to capture the thermal footprint of the evaporating droplet. Four electric fields were characterised; 0, 5, 10 and 11 kV/cm. As the electric field is increased the contact angle was observed to decrease. The local heat flux profile, peak and radial location of this peek were observed to be independent of the applied electric field for all test points for this working fluid and surface combination.

1. Introduction

Heat and mass transfer to a sessile evaporating droplet has been an area of growing interest due to its increasing use in industrial applications and processes. Previous research has primarily focused on heat transfer enhancement by investigating varied substrate structures and coatings and their impact on droplet wettability, the triple line and the average convective heat flux [1, 2, 3, 4, 5]. Droplet evaporation is governed by a number of different physical phenomena: heat transfer by convection, heat transfer induced by the substrate conduction, diffusion of the vapour around the droplet in the gaseous phase, and the molecular interactions between the droplet and the substrate that change the wettability of the evaporating droplet [6].

When a sessile droplet is exposed to a static electric field, its shape is defined by the balance

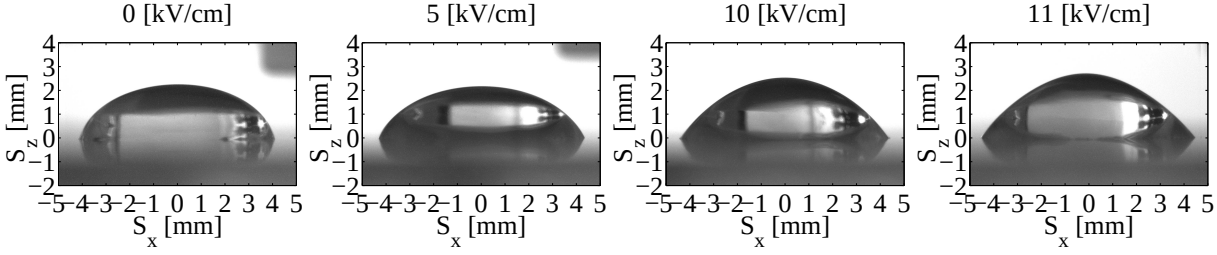

Figure 1: Sessile water droplet shape for a increasing applied electric field.

of surface tension, electrostatic and gravitational forces. The surface tension component tends to make the droplet spherical, the electrostatic force elongates the droplet towards the source electrode and the gravitational "flattens" the droplet. The degree by which the droplet elongates is dependent on the intensity of the electric field. This fact is highlighted in Fig 1.

The evaporation of a sessile droplet in an electric field is still a largely underdeveloped topic. Takano et al. [7] explored the average heat flux enhancement for varied substrate temperatures above the Leidenfrost temperature of the working fluid. Their experimental configuration consisted of the source electrode being placed below an insulated substrate. The droplet was placed on this substrate and was connected to a ground electrode. Two working fluids were investigated; Ethanol and R-133. They observed a peak enhancement ever the reference case of no applied voltage of 7.6× for the ethanol droplet at an applied voltage of 250 V and 2.8× for the R-113 case at an applied voltage of 2000 V.

The local convective heat flux in the region of the triple line, where the solid - liquid - vapour phases interface is a key physical problem not yet fully solved. The liquid thickness in this zone is of the micron to nanometer scale [8]. The purpose of this research is to investigate the impact that a static electric field of varied strength has on this region and the subsequent local convective heat flux in this region and across the entire evaporating droplet.

2. Experimental Apparatus and Data Reduction

The experimental apparatus consists of three primary components; the heat transfer section, the electric field droplet evaporation and imaging system. These are illustrated in the rig schematic in Fig 2.

2.1. Heat transfer section

The thermal exchange surface consists of a 25 µm thick, 140×80 mm^2 Goodfellow Stainless Steel 316 (Fe/Cr18/Ni10/Mo3) foil. The foil is clamped between two copper bus bars, both bus bars are electrically connected to a Lambda GENESYS $6 - 200$ D.C. power supply. The copper bus bars are mounted to a polyrtheretheketone (PEEK) housing. This PEEK housing is shown in Fig 2a. A tensioning system is employed in order to counteract foil warping at higher wall heat fluxes. One set of bus bars are rigidly fixed to the PEEK housing while the other is spring loaded. The 25 µm foil is stretched across a central $140 \times 100 \times 13$ mm^3 PEEK piece. This configuration is highlighted in Fig 2b.

The central PEEK piece serves to house a $70 \times 70 \times 2$ mm^3 infrared (IR) transparent Calcium

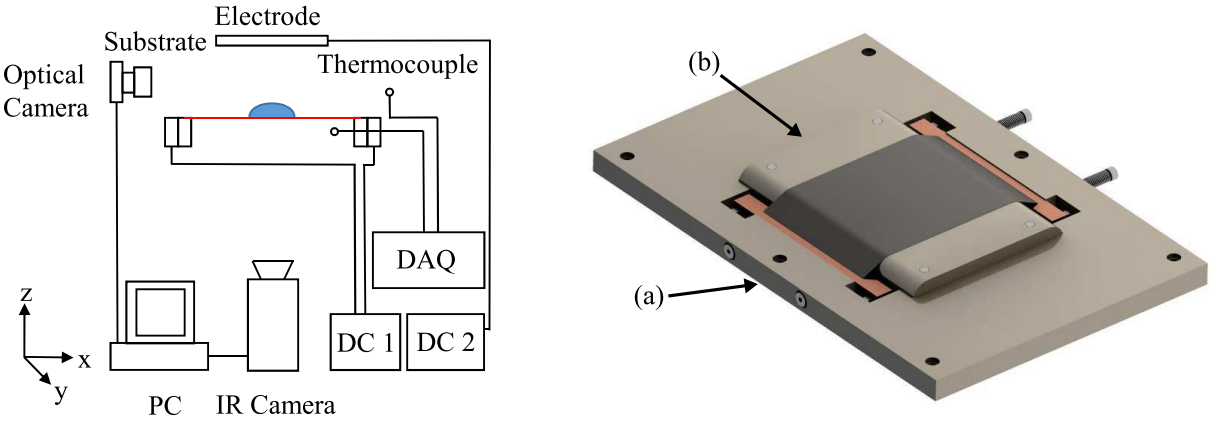

Figure 2: Experimental rig schematic and Thermal exchange surface. (a) PEEK housing and (b) Central PEEK piece.

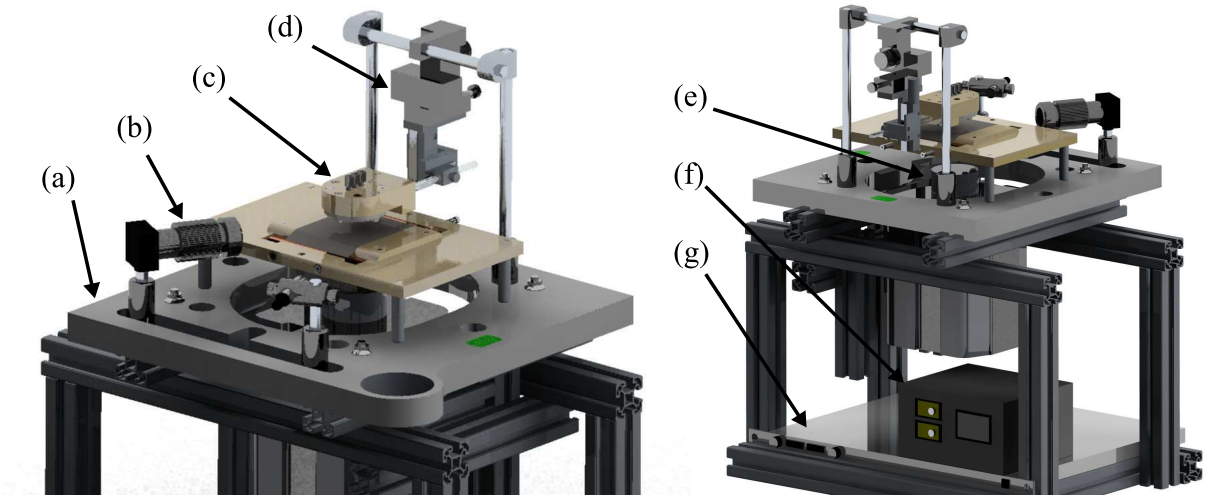

Figure 3: Experimental set-up. (a) Ertacetal baseplate, (b) Optical camera. (c) Electrode, (d) XYZ micropositioner stage, (e) Thermal Imaging camera, (f) Profector system, and (g) DC power supply

Fluoride (CaF_2) glass. The top of this IR glass is positioned 7 mm below the underside of the foil. This configuration establishes a $71 \times 71 \times 7$ mm^3 air cavity. During experimentation this trapped air acts as a thermal barrier, ensuring that the heat lost through conduction on the underside of the foil is minimised. A 1.6 mm exposed T-type thermocouple is used to measure the air temperature at the midpoint of the air gap cavity. The underside of the foil is exposed for direct temperature measurement by an infrared camera. It is coated with a thin layer of matt black paint of known emissivity, this is to facilitate accurate temperature measurement.

2.1.1. Material Properties The foil and paint properties are outlined in Table 1. The paint thickness was determined using a Dektak 6m programmable surface profiler. The foil properties were defined using the supplied Goodfellows data sheet, while the paint layer was determined from data tabulated by Donoghue [9], Sundqvist [10] and Raghu and Philip [11].

Table 1: Foil, paint and IR properties properties.

Foil thickness, δ_f	25	µm	Paint layer thickness, δ_p	10.52	µm
Density, ρ_f	7960	kg/m^3	Density, ρ_p	1162	kg/m^3
Thermal conductivity, k_f	16.3	W/m K	Thermal conductivity, k_p	0.57	W/m K
Specific heat, $C_{p,f}$	390	J/kg K	Specific heat, $C_{p,p}$	2835	J/kg K
CaF_2 Emissivity, ε_{CaF_2}	.25		Paint Emissivity, ε_p	.95	

2.2. Droplet Evaporation System
The thermal exchange section is mounted on a Ertacetal baseplate (see Fig 3a), $400 \times 320 \times 30$ mm^3, and is supported on 40×40 mm^2 Rexroth aluminium profile frame. The applied electrode voltage is supplied and controlled by a Profector life science system. The Profector system can supply between 0 – 30 kV DC voltage at 0.01 kV increments. The source electrode is 5 mm thick stainless steel disc with a diameter of 55 mm. A XYZ micro

positioner is implemented to control placement of the source electrode. The separation height can be accurately set to $\pm$ 0.5 µm. The droplet volume was controlled using a KD Scientific 200 syringe pump and a Hamilton 1750 Gastight 500 µl syringe.

2.3. Imaging system

The imaging system consisted of two parts; a Chameleon CMLN-1352M optical camera and a FLIR SC6000 thermal imaging camera. Both cameras are controlled by a dedicated computer. The optical camera is mounted to the Ertacetal baseplace as shown in Fig 3b. It was used to focus on the evaporating droplet and to define droplet shape and volume during testing.

A FLIR SC6000 high resolution, high frame rate IR camera was used to capture the thermal footprint of the evaporating droplet. The camera is mounted to the aluminium profile, directly below the thermal exchange surface as shown in Fig 3e. The IR camera is fitted with a 25 mm lens. The frame rate and capturing period is controlled via an external pulse generated by a National Instruments (NI) 9263 Data Acquisition Module (DAQ) in LabVIEW. The thermal camera is set to record an image that is 400×400 pixels at a speed of 200 Hz, with each pixel corresponding to a width of 160 µm. After a test is completed the acquired raw data is exported in a .sfmov file extension and is later processed in MATLAB.

2.4. Experimental parameters

Four average electric fields were examined; 0, 5, 10, and 11 kV/cm. The droplet volume and electrode separation height was set to 80 µl and 10 mm respectively for all test points. The working fluid used was deionised water from Sigma-Aldrich, with a boiling point of 100°C. Experiments were conducted at atmospheric pressure and room temperature. The substrate temperature was assumed to be uniform across its thickness for a constant heat flux input of ≈ 970 W/m^2 for all test points. This corresponded to a surface temperature (T_shaha) of ~ 70°C in steady state conditions.

2.5. Experimental procedure

Prior to testing the 80 µl deionised water droplet is placed in the centre of the stainless steel substrate. The electrode is positioned concentrically above the droplet at the outlined separation height. The start of testing is triggered using an in-house developed LabVIEW program. Once the program is started it triggers the thermal imaging camera, optical camera and foil power supply, while simultaneously acquiring thermocouple, foil voltage drop and circuit current readings. Data is acquired for 1 second every 60 seconds for each test. The total test time for all tests is 20 minutes. This results in 21 sub-points per test, with each sub-point separated by 59 seconds. The acquisition timing sequence is outlined in Fig 4. All droplets were completely evaporated by the completion of each test.

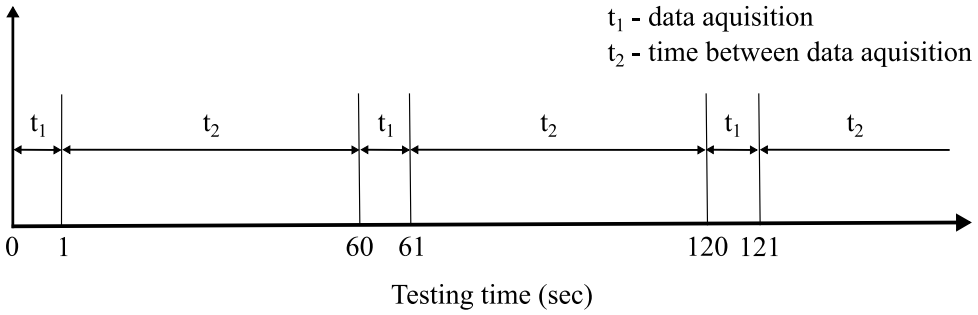

Figure 4: Data acquisition timeline

2.6. Data analysis and processing
The captured thermal images are then processed using MATLAB. Processing of this data can be divided into three phases; image correction, heat transfer analysis and averaging.

2.6.1. Image correction The captured .sfmov video file is imported into MATLAB. Each image is extracted and the bad pixel, gain, offset and counts to temperature conversion are applied. This results in 200 400×400 thermal images stored in a 3D array per sub-point or 4,200 400×400 images per test.

2.6.2. Heat transfer analysis In order to compute the thermal energy convected to the evaporating droplet, various fluid, foil and paint properties (see Table 1) are input along with relevant calibration curves for the ambient air and the air cavity. In order to evaluate the thermal energy convected by the evaporating droplet, an element by element based energy balance is applied to each pixel of the recorded thermal image. The energy balance can be defined as [12]:

$$\dot{E}_{in} + \dot{E}_{gen} - \dot{E}_{out} = \dot{E}_{st} \tag{1}$$

It is assumed that there is uniform heat generation within the foil, the temperature through the thickness of the foil is constant as Bi $\ll 1$ for both the paint and foil layers. This results in the following expression for the convective heat flux due to droplet evaporation, q''_{DE}:

$$q''_{DE} = q''_{gen} - q''_{cond} - q''_{rad,b} + (k_f\delta_f + k_p\delta_p)\left(\frac{\partial^2 T}{\partial x^2} + \frac{\partial^2 T}{\partial y^2}\right) - (\rho_f C_{p,f}\delta_f + \rho_p C_{p,p}\delta_p)\frac{\partial T}{\partial t} \tag{2}$$

where q''_{gen} is the heat flux generated in the foil by Joule heating given by Eq 3a. The second term on the RHS accounts for heat lost through conduction across the air gap cavity and is given by Eq 3b, where k_{ag} is the thermal conductivity of the bulk fluid (air) and dT/dz is the temperate gradient across the air gap to the IR window. $q''_{rad,b}$ is the total radiative emission from the underside of the foil to the top of the IR transparent CaF_2 glass and is given by Eq 3c. The fourth term in Eq 2 refers to heat transfer due to lateral conduction. The partial derivative is solved by means of a central-difference approach using the inbuilt `del2` MATLAB function. The final term accounts for the energy stored within the foil between images, also known as the capacitance term. This is found using the `gradient` function.

$$q''_{gen} = \frac{I_s V_s}{A_s}; \qquad q''_{cond} = -k_{ag}\frac{dT}{dz}; \qquad q''_{rad,b} = \frac{\sigma\left(T_s^4 - T_{CaF_2}^4\right)}{1/\varepsilon_p + 1/\varepsilon_{CaF_2} - 1} \tag{3}$$

2.6.3. Averaging The final stage of processing is to average all images over each sub-point. This assumes that the droplet evaporation is quasi-steady during the 1 second capture period. This assumption is shown to be valid due to the relatively low calculated energy storage term. The radial profile of the convective heat flux is then found by taking a line radially from the centre of the convective heat flux map in 1° increments and averaging the results. An example of this resultant profile can be seen in Fig 5.

3. Results and Discussion
Fig 5 illustrates an example of the processed droplet evaporation data. In this case a droplet with an initial volume of 80 µl is evaporating on the heated stainless steel substrate and is experiencing an average static applied electric field of 11 kV/cm. This measurement corresponds to 4 minutes from the start of the test. The altered droplet shape due to the applied electric field is shown in

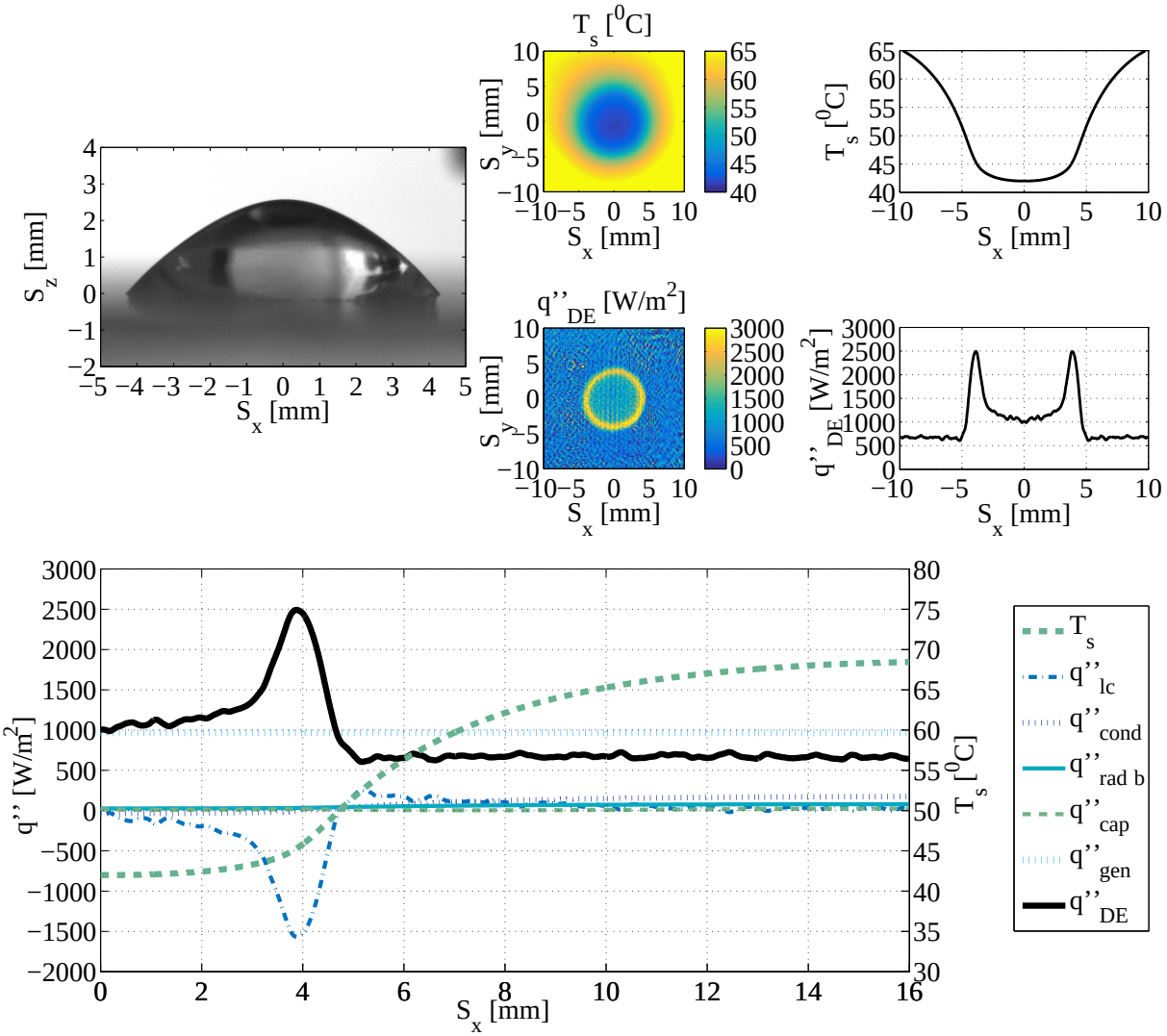

Figure 5: Sample processed data. E = 11 kV/cm, t = 4 min, v = 80 µl

the top left of the figure. Its corresponding temperature map and profile (top) and convective heat flux map and profile (middle) are shown on the top right of the figure. From the convective heat flux map it can be observed that the greatest region of cooling occurs in a ring around the edge of the droplet near the triple contact line. This is due to the high evaporation rate in the region around the triple line, and is similar to that observed by Marchuk et al. [8] in their investigation of the local heat flux characteristic of an evaporating droplet in no electric field. This profile shape is determined through the inclusion of the lateral conduction term (q''_{lc}) to satisfy the Cauchy problem of the energy balance by accounting for energy movement within the foil. The averaged radial profile of this lateral conduction term and all other local energy balance terms are shown at the bottom of Fig 5.

The final plot in Fig 5 highlights the individual terms of the energy balance in solving for the convective heat flux (q''_{DE}). The secondary axis refers to the radial temperature profile of the foil surface. A peak local convective heat flux of 2,493 W/m^2 is noted at a radial distance of 3.88 mm from the centre of the droplet for this example. Both the energy generation term (q''_{gen}) and storage term (q''_{cap}) remain constant at 967.3 W/m^2 and $\approx$ 0 W/m^2 respectively as

the radial distance from the droplet centre (S_x) increases. In the case of q''_{gen} this is due to the uniform heat generation, foil and paint thickness across the foil. The averaged radial profile of $q''_{cap} \approx 0$ W/m^2 for all values of S_x further demonstrates the quasi-steady state nature of the process.

Examining each term moving radially outward from the centre of the droplet ($S_x = 0$ mm) for $S_x = 0 - 2$ mm it can be seen that the magnitude of $q''_{DE} \approx q''_{gen}$. This is due to the low temperature gradient across this region (0.215°C/mm) resulting in a small q''_{lc}. Similarly, the low temperature value of the foil (≈ 40.2°C) results in negligible heat losses (conduction (q''_{cond}) and radiation to the IR glass ($q''_{rad,b}$)) across the air gap. Increasing S_x further to between $3 - 5$ mm, i.e. the region around the triple line of the droplet, the point of highest local convective heat flux for q''_{DE} is measured. As in the previous case q''_{cond} and $q''_{rad,b}$ are small in this region. The energy balance in this section is dominated by q''_{lc} due to the large temperature gradient in this area (4.16°C/mm) caused by the high evaporative convective heat flux. Finally from $6 - 16$ mm the convective term q''_{DE} is observed to remain relatively constant at ≈ 700 W/m^2. q''_{lc}1-+ ≈ 0 W/m^2 in this range due to the low temperature gradient (1.21°C/mm). Both the q''_{cond} and $q''_{rad,b}$ terms, ≈ 174 W/m^2 and ≈ 79 W/m^2 respectfully, are small but not negligible in this region due to the radially increasing temperature. Thus q''_{DE} is marginally smaller than

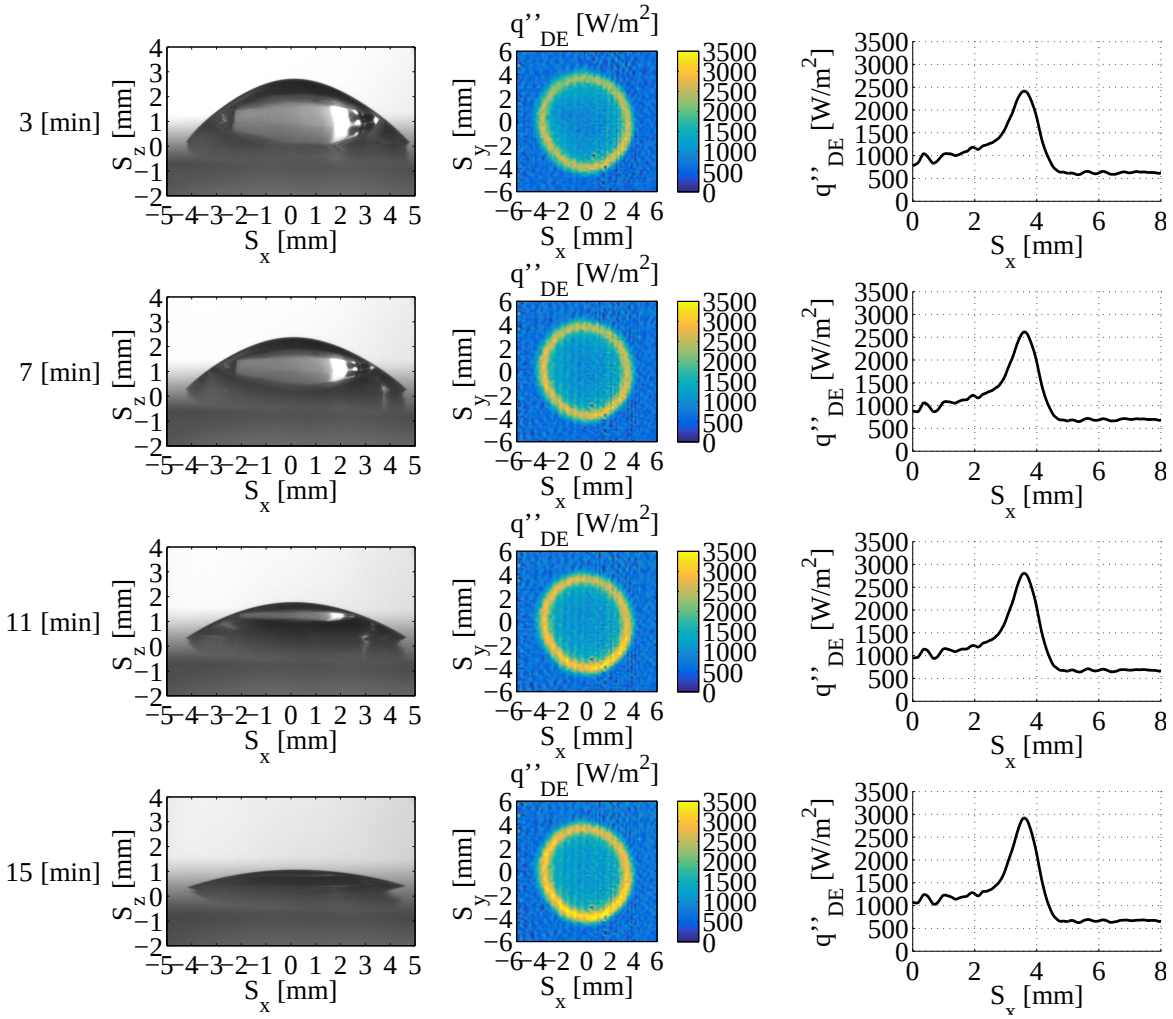

Figure 6: Droplet evaporation for increasing time in an 11 kV/cm static electric field

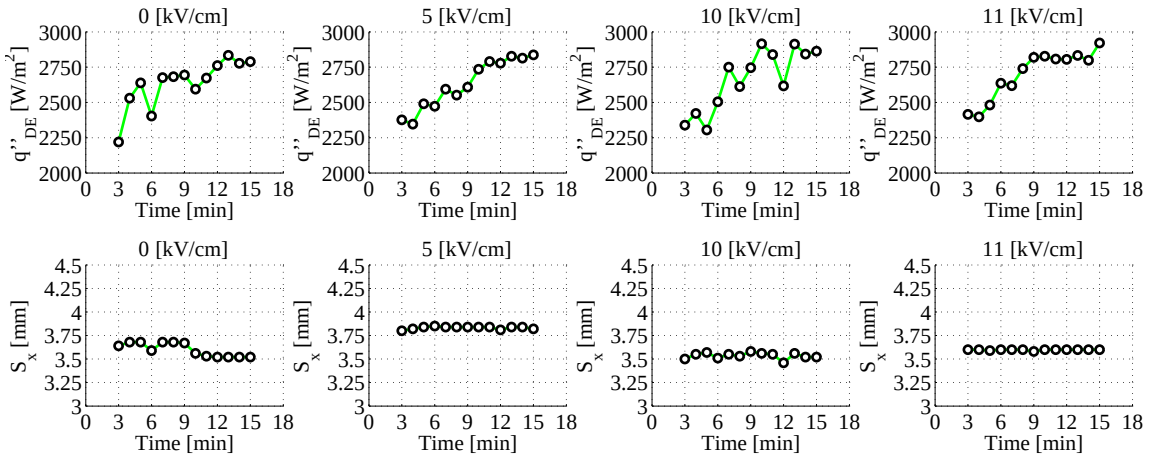

Figure 7: Peak convective heat flux and radial position of the peak for increasing time

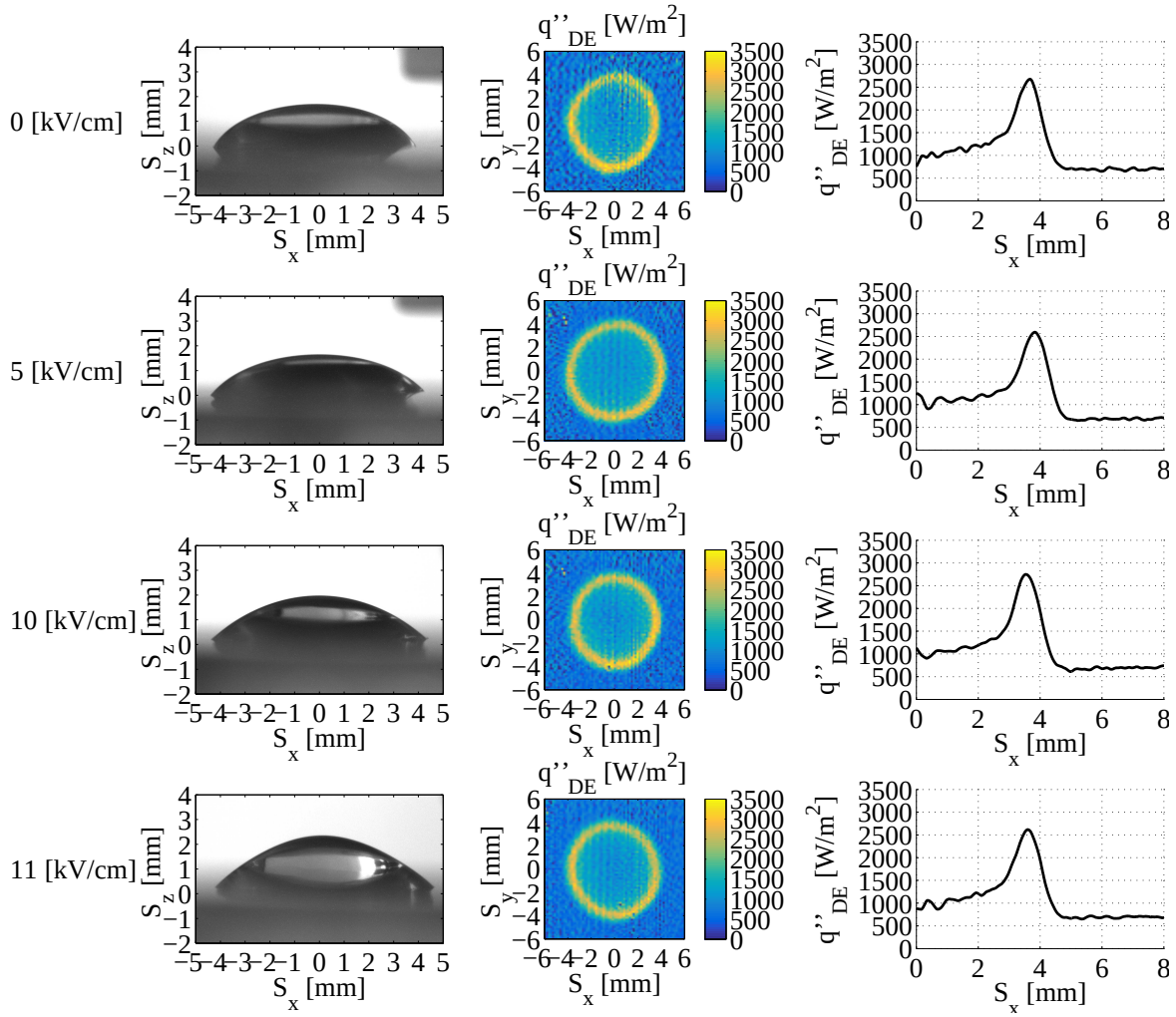

Figure 8: Droplet evaporation at 4 minutes for an increasing static electric field

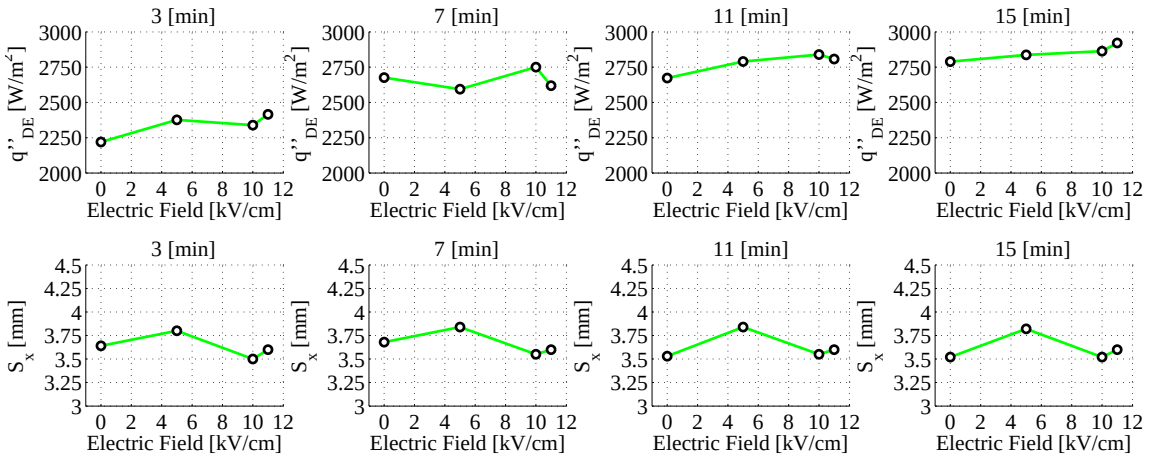

Figure 9: Peak convective heat flux and radial position of the peak for increasing applied electric field

q''_{gen}, with q''_{DE} denoting the cooling due to natural convection from the top surface to the air surrounding the droplet across this range. This result for q''_{DE} is incorporated into Fig 6.

3.1. Local convective heat flux characteristics over time

Fig 6 shows the development of the local convective heat flux profile over time as the sessile droplet evaporates in the applied electric field. The first column shows the shape of the evaporating droplet over time, with columns two and three highlighting the convective heat flux map and profile of the evaporating droplet. From column one it can be seen the droplet is "pinned" during testing. From columns two and three it can be observed that the peak convective heat flux increases marginally as the droplet evaporates, while maintaining a near identical profile shape and radial location of this peak. These points are further highlighted in Fig 7.

Fig 7 demonstrates how the peak local convective heat flux (top row) and its radial position (bottom row) change across each test as the droplet evaporates. From results it is clear that the peak convective heat flux increases over time as the liquid volume diminishes. However, there is no significant influence of the electrostatic field on the peak heat flux. In fact, the pinning of the triple contact line results in a radial location of the peak heat flux that does not vary with time nor be influenced by the electric field. This fact is clearly shown in Fig 9.

3.2. Local convective heat flux characteristics for varied electric field

Fig 8 shows the development of the local convective heat flux profile for a range of applied electric fields 4 minutes into each test. As in Fig 6 the first column shows the shape, while columns two and three highlight the convective heat flux map and profile for the evaporating droplet. The electric field intensity increases per row. The impact of the applied electric field can be clearly observed in column one. With a decreasing droplet contact angle as the electric field is increased. From columns two and three it can be seen that the convective heat flux profile is largely independent of the applied electric field.

Fig 9 demonstrates how the peak local convective heat flux (top row) and its radial position (bottom row) change for different applied electric fields. Like the convective heat flux profile the peak convective heat flux and its radial location are also observed to be independent of the applied electric field.

4. Conclusion

The experimental results show that the cooling profile, the peak convective heat flux, and the radial location of this peak are independent of the applied electric field for our results of an evaporating water droplet for the conditions of these particular experiments. Due to the pinning of the droplet during testing no change in any of the aforementioned parameters was noted as each test progressed through time. In moving forward we will investigate the overall heat balance of the evaporating droplet and the local convective heat flux in the non - pinned case to contrast and compare the two cases both with and without electric fields.

Acknowledgements

The authors would like to acknowledge the financial support of the Irish Research Council (IRC).

References

[1] Picknett R and Bexon R 1977 *Journal of Colloid and Interface Science* **61** 336 – 350 ISSN 0021-9797
[2] Sobac B and Brutin D 2011 *Langmuir* **27** 14999–15007
[3] Semenov S, Starov V, Rubio R, Agogo H and Velarde M 2011 *Colloids and Surfaces A: Physicochemical and Engineering Aspects* **391** 135 – 144 ISSN 0927-7757 18th International Symposium on Surfactants in Solution (SIS)
[4] Dunn G, Wilson S, Duffy B, David S and Sefiane K 2008 *Colloids and Surfaces A: Physicochemical and Engineering Aspects* **323** 50–55
[5] David S, Sefiane K and Tadrist L 2007 *Colloids and Surfaces A: Physicochemical and Engineering Aspects* **298** 108 – 114 ISSN 0927-7757 {XVIIth} European Chemistry at Interfaces Conference
[6] Vancauwenberghe V, Di Marco P and Brutin D 2013 *Colloids and Surfaces A: Physicochemical and Engineering Aspects* **432** 50–56
[7] Takano K, Tanasawa I and Nishio S 1994 *International Journal of Heat and Mass Transfer* **37, Supplement 1** 65 – 71 ISSN 0017-9310
[8] Marchuk I, Karchevsky A, Surtaev A and Kabov O 2015 *International Journal of Aerospace Engineering* **2015**
[9] Donoghue D B, Albadawi A, Delauré Y M C, Robinson A J and Murray D B 2014 *International Journal of Heat and Mass Transfer* **71** 439–450
[10] Sundqvist B 1992 *Journal of applied physics* **72** 539–545
[11] Raghu O and Philip J 2006 *Measurement science and technology* **17** 2945
[12] Bergman T L, Incropera F P and Lavine A S 2011 *Fundamentals of heat and mass transfer* (John Wiley & Sons)